

RESEARCH ARTICLE | MARCH 04 2024

Characterization of experimental and simulated micrometer-scale soft x-ray-emitting laser plasmas: Toward predictive radiance calculations ^{EP}

Special Collection: [Plasma Sources for Advanced Semiconductor Applications](#)

K. Mongey  ; S. J. J. de Lange  ; R. Brady  ; D. J. Hemminga  ; B. Delaney  ; M. M. Basko  ; E. Sokell  ; F. O'Reilly  ; J. Sheil  

 Check for updates

Appl. Phys. Lett. 124, 102104 (2024)

<https://doi.org/10.1063/5.0190309>



01 July 2024 10:54:09



Applied Physics Letters

Special Topic:

Quantum Networks

Guest Editors: David Awschalom, Ronald Hanson, Stephanie Simmons

[Submit Today!](#)

Characterization of experimental and simulated micrometer-scale soft x-ray-emitting laser plasmas: Toward predictive radiance calculations

Cite as: Appl. Phys. Lett. **124**, 102104 (2024); doi: [10.1063/5.0190309](https://doi.org/10.1063/5.0190309)

Submitted: 5 December 2023 · Accepted: 13 February 2024 ·

Published Online: 4 March 2024






View Online



Export Citation



CrossMark

K. Mongey,^{1,2}  S. J. J. de Lange,^{2,3}  R. Brady,¹  D. J. Hemminga,^{2,3}  B. Delaney,¹  M. M. Basko,⁴  E. Sokell,¹ 
F. O'Reilly,¹  and J. Sheil^{2,3,a)} 

AFFILIATIONS

¹School of Physics, University College Dublin, Belfield, Dublin 4, Ireland

²Advanced Research Center for Nanolithography, Science Park 106, 1098 XG Amsterdam, The Netherlands

³Department of Physics and Astronomy, and LaserLaB, Vrije Universiteit Amsterdam, De Boelelaan 1081, 1081 HV Amsterdam, The Netherlands

⁴Keldysh Institute of Applied Mathematics, Miusskaya Square 4, 125047 Moscow, Russia

Note: This paper is part of the Special Topic: Plasma Sources for Advanced Semiconductor Applications.

a) Author to whom correspondence should be addressed: j.sheil@arcnl.nl

ABSTRACT

Experimentally generated and simulated soft x-ray plasma images and spectra from 1064 nm-driven laser-produced plasmas from slab tin are presented. Produced are small, micrometer-scale emission volumes with principle imaged emission lying between 1.2 and 2.5 nm. Experimental images of the soft x-ray emission of these plasmas are generated using a pinhole imaging system, which enables spatial characterization of the plasmas, and a simple transmission grating spectrometer with a 100 nm pitch grating is used to facilitate the spectral characterization of these plasmas. Plasmas are simulated under similar experimental conditions to those used with the single-fluid, single-temperature radiation-hydrodynamics code RALEF-2D. Coupling the simulation output with optical modeling methods demonstrates its promise as a capability for modeling the spatial and spectral behavior of soft x-ray-emitting tin plasmas at such scales and laser energies.

© 2024 Author(s). All article content, except where otherwise noted, is licensed under a Creative Commons Attribution (CC BY) license (<http://creativecommons.org/licenses/by/4.0/>). <https://doi.org/10.1063/5.0190309>

High-temperature plasmas containing multiply ionized ions, such as those created by intense laser irradiation of solid, liquid, and gaseous targets, are powerful sources of short-wavelength radiation.^{1–3} Their compact nature coupled with the relative ease with which the emission wavelength and intensity can be tuned (realized by a judicious choice of laser wavelength, pulse length, energy, focusing properties, and target material) justifies their deployment in numerous scientific and industrial disciplines requiring short-wavelength radiation.^{4,5} The most extensively studied, highest average power laser plasma short-wavelength light source are extreme ultraviolet (EUV) emitting tin plasmas adapted for semiconductor manufacturing.^{6,7} The 13.5 ± 0.135 nm optimized radiation generated in such plasmas is used to print nanometer-scale patterns on silicon wafers in current industry-leading nanolithography foundries. Spectral characterization of such tin plasmas at and below^{8,9} 13.5 nm provides fundamental insights into their radiative behavior,

which can fuel source optimization for industrial applications. Related to this, the analysis of nanometer-scale defects on wafers can also utilize short wavelength plasma emission, and the research, development, and testing of these sources is ongoing^{10–12} and benefits from continued spectroscopic studies of laser-produced plasma (LPP) soft x-ray radiation (SXR) sources.^{13–16}

Laser-driven SXR sources have also been employed as light sources for water window (2.28–4.37 nm) soft x-ray tomography.^{17–21} For example, laser-driven SXR generating molybdenum plasmas have been used to image biological cells at resolution comparable to those recorded using synchrotron radiation,²² operating at a fraction of the cost of such large-scale facilities. Many applications mentioned above have etendue-limiting bottlenecks, such as required illumination coherence/magnification/detector size limits, or monochromator input slit size/acceptance angle limits. In these low-etendue applications, there is often an inverse quadratic coupling efficiency relationship with

the plasma emission diameter. The challenge, therefore, lies in maximizing the *radiance* of these sources, i.e., the ratio of SXR flux to the emitting area. Driving larger photon fluxes from lengthscales plasmas requires a detailed understanding of plasma formation, evolution, and radiative behavior on short lengthscales. This can be realized by coupling well-characterized spatial and spectral measurements of such tiny soft x-ray plasmas with their detailed simulation.

The goal of this paper is to characterize, using detailed experimental measurements and radiation-hydrodynamic (RHD) simulations, the radiative properties of small-scale laser plasmas relevant to the aforementioned applications. The utility here lies in the comparison of spatial imaging and spectral characterization of the experimentally recorded soft x-ray emission with the predictions of RHD simulations at small scale. Studies involving modeling soft x-ray plasma emission²³ have been performed, but at larger spatial scales and higher laser power densities. From experimental and simulation avenues, we report the following: (i) the existence of an intense emission feature at 1.8 nm, with moderate emission also present at 1.5 nm and at 2.4 nm; (ii) ion stages from Sn²²⁺ to Sn²⁸⁺ are the dominant contributors across all laser pulse energies leading to similar spectral profiles; and (iii) the adequacy of a RHD code for simulating soft x-ray-emitting LPPs, which can facilitate the evaluation of the actual soft x-ray plasma size. The benchmarking of RHD simulations with experimental measurements through comparisons of spectra and plasma images forms a large part of this manuscript's focus. Such a modeling capability could reliably predict, over a broad parameter space, plasma behavior in situations that are not easily probed with experimental diagnostic methods and, importantly, be used to quickly identify optimal source conditions. As well as obtaining fundamental insight into the behavior of these plasmas and their relevance to the semiconductor industry and applications outlined above, we select tin as the target of choice for two reasons: (i) because there exists high-quality radiative data (opacity, emissivity) of tin plasmas, data that have been incorporated into radiation-hydrodynamic simulations for the purpose of EUV source modeling,^{24,25} and (ii) the observation of intense soft x-ray emission from laser-driven tin plasmas at similar experimental power densities used in this work. The observed spectral features have been identified and are attributed to transitions in open *3d* subshell ions.^{26,27} Additionally, the behavior of such imaged volumes at the scales and wavelengths presented is largely unexplored. At these sizes, optical depth effects are minimized, providing a simple, foundational case for comparison.

In the experiments, slab tin targets were irradiated with Nd:YAG $\lambda = 1064$ nm laser pulses with measured Gaussian temporal profile of 5 ns full width at half maximum (FWHM). The pulses were focused onto the target using a 20 mm diffraction-limited focal length aspheric lens.²⁸ The resulting soft x-ray plasma emission volumes were imaged at focus using a pinhole with a measured diameter of $4.3 \mu\text{m}$ in combination with an aluminum filter of thickness 660 ± 60 nm. This is shown in Fig. 1(a). An IDS U3 3682XLE-NIR CMOS camera²⁹ with a $2.2 \mu\text{m}$ pixel size served as the photon detector. A glass window in front of the detector was removed to prevent attenuation of the incident soft x-rays. The pinhole shown to scale in Fig. 1(b), has an average measured diameter of $4.3 \mu\text{m}$. The aluminum filter has a high extinction coefficient for visible and infrared light,³⁰ which is particularly important in attenuating laser light scattered by the plasma.

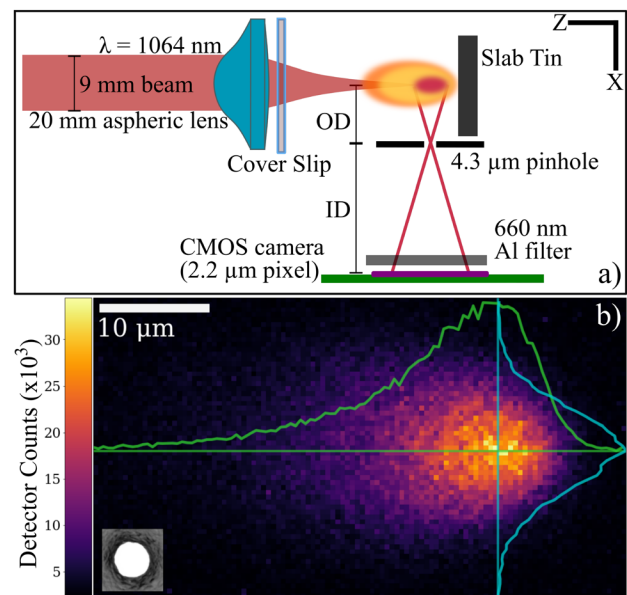


FIG. 1. (a) Schematic of the experimental setup for soft x-ray imaging of laser-produced plasmas. (b) Plasma image recorded with a laser energy of 60 mJ. The cyan and green curves show lineouts taken parallel and perpendicular to the target, respectively. The inset in panel (b) shows an SEM image of the $4.3 \mu\text{m}$ -diameter pinhole shown on the same scale as the plasma image.

The laser spatial profile was characterized using an equivalent CMOS detector to that described earlier with infrared attenuating optics and notch filter to measure exclusively the laser profile. This optical system yielded a $D4\sigma$ focal spot diameter of $25 \mu\text{m}$ at the tightest focus along each principal axis measured using the method outlined in ISO 11146,³¹ with a broadly Lorentzian shape. The quantum efficiency of the camera was not measured, however, it likely possesses a shape similar to that reported by Harada *et al.*;³² it is expected to vary by approximately $\pm 10\%$ across the considered wavelength range, and so we have assumed it to be flat in the modeling presented in the following. In line with previous measurements of the camera spectral resolution,³³ we determine a value of approximately 80 eV based on photon counting from photons of a known wavelength in the region. Emission features below 0.6 nm could be observed; however, no such features were observed in any recorded soft x-ray spectra. This sets a lower bound for both imaging and simulations. From CXRO models of soft x-ray transmission,³⁴ the throughput of a 660 nm-thick aluminum foil drops below 5% at 3.5 nm. This sets the upper wavelength limit for our experimental spectra, images, and simulation model.

Plasmas were formed by ablating slab tin with laser energies of 8, 20, 40, and 60 mJ, corresponding to power densities of 0.3, 0.8, 1.6, and $2.4 \times 10^{12} \text{ W cm}^{-2}$ in vacuum with background pressure $\sim 10^{-5}$ mbar. A typical plasma image is shown in Fig. 1(b). It has a characteristically skewed emission profile perpendicular to the target, with a near-normal emission distribution parallel to the target that peaks on the laser axis. Sample experimental (and simulated) soft x-ray spectra are shown in Fig. 2. The spectrum derived from the pinhole (blue) was recorded using a laser energy of 8 mJ to avoid photon

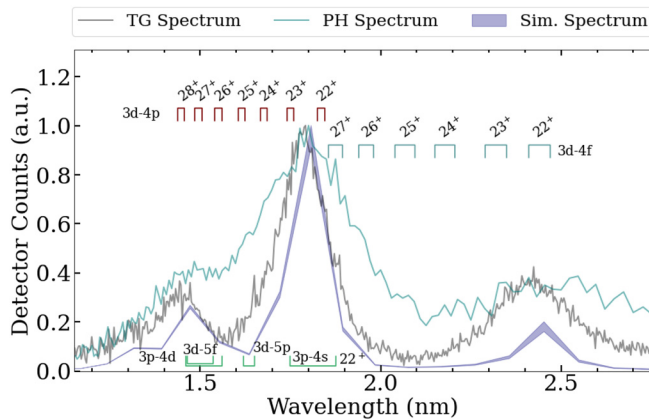


FIG. 2. Comparison of both experimental pinhole (PH) and transmission grating (TG) spectrometer spectra in blue and gray, respectively, and a simulated spectrum in purple. The simulated spectrum is a one-dimensional emission spectrum predicted by RALEF-2D convolved with the impulse response function (IRF) of the transmission grating spectrometer, with uncertainties in the IRF captured in the shaded region. Emission regions of tin charge stages, Sn^{22+} – Sn^{28+} , are indicated alongside the transition array type identified by Burkhalter *et al.*²⁶

pileup in the detector. The emission in this spectral range was corroborated using a home-built transmission grating spectrometer, recorded at a higher power density and shown in gray in Fig. 2. These spectra do not change significantly over the range of power densities used. Strong emission features between 1.2 and 2.5 nm were observed in all spectra. In order to characterize the size of the plasma image, the magnification of the pinhole imaging system was determined by driving the target and lens co-directionally by equal, known amounts (between 15 and 60 μm) in the Z direction (see Fig. 1(a)) using bespoke 1.5 μm -accuracy stepper motors and subsequently recording plasma images. The resulting movement of the plasma image on the camera was recorded, and taking the ratio between this distance and the known driven motor distance yielded an average magnification of 4.9 ± 0.2 . To determine the object distance, the camera was moved in the X direction away from the plasma, and, at each camera position, the magnification was calculated. Given that the magnification increases linearly with distance, the object distance could be determined with a linear relation yielding $O_D = 8.7 \pm 0.7$ mm. The magnification of the spectrometer was determined similarly.

To better understand the experimentally recorded plasma images and spectra, we performed two-dimensional (2D) radiation-hydrodynamic simulations using the RALEF-2D code,^{35,36} an acronym for Radiation Arbitrary Lagrangian Eulerian Fluid dynamics in two dimensions. RALEF-2D is a single-fluid, single-temperature radiation-hydrodynamic code, iterating on the hydrodynamic code CAVEAT³⁷ by including thermal conduction and radiation transport, both of which are implemented using a symmetric semi-implicit method with respect to time discretization.^{38,39} RALEF-2D employs a hybrid laser deposition model,⁴⁰ which utilizes geometrical ray tracing and the 1D solution of the Helmholtz wave equation. RALEF-2D solves the radiation-hydrodynamic equations on a structured, quadrilateral mesh with a second-order Godunov-type scheme.

Here, simulations were performed on a strictly Eulerian rectangular mesh, for each of the four experimental power densities with a fit to the measured laser spatial profile and temporal profile serving as model input. In Fig. 3, we show the RALEF-2D prediction of the net radiated power in the 0.62–3.26 nm range per unit volume, or instantaneous emission profile, at $t = 7.5$ ns for the 60 mJ simulated case. Also shown is the computational grid, the spatial variation of the free electron density (up to the critical electron density of approximately $1 \times 10^{21} \text{ cm}^{-3}$) and average charge stage contours. The opacity data used in RALEF-2D is generated by the THERMOS code⁴¹ and is tailored to critical electron densities of $\sim 10^{19} \text{ cm}^{-3}$. With a 20 mm focal length lens and a beam diameter before focusing of 9 mm at the lens front, a laser with M2 of 3.5 yields a Rayleigh range $z_R = 20 \mu\text{m}$. The implementation of such irradiation conditions in RALEF-2D calls for the incorporation of beam refraction during simulations, but as the spatial profile of the laser tends toward the scale of the laser wavelength ($\sim 1 \mu\text{m}$) spurious self-focusing of the laser beam on-axis occurs, which ultimately yields nonphysical output. To circumvent this, we utilized a cylindrical beam of constant spatial profile equivalent to that of the laser profile in focus at the target. The majority of the laser deposition occurs in the region in front of the critical electron density surface, which lies close to the target surface during the simulation.

Two independent approaches were used to benchmark the RHD simulations. This first method consists of comparing soft x-ray images recorded in the experiments [e.g., Fig. 1(b)] to that predicted by RALEF-2D, and the second involves comparing experimental spectra

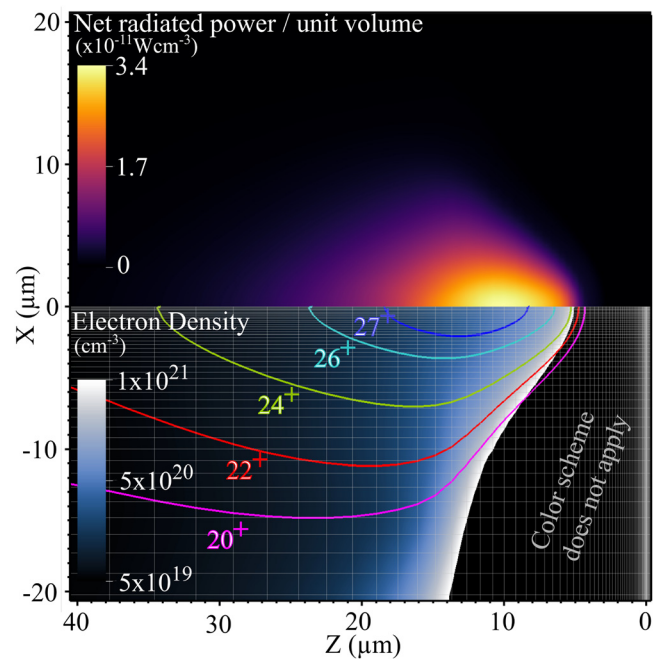


FIG. 3. Simulated plasma profiles. A 60 mJ laser pulse is incident from the left on a flat tin target placed at $Z \leq 0 \mu\text{m}$. The upper panel shows the instantaneous net radiated power per unit volume in the 0.62–3.26 nm wavelength range at $t = 7.5$ ns (peak laser power). The lower panel shows the electron density superimposed atop the simulation grid. Lines of constant average charge state $20^+ \leq Z \leq 27^+$ are indicated by the various colors.

(e.g., Fig. 2) to simulated spectra. The first method involves the use of 28 discrete, unevenly spaced wavelength groups extending from 0.6 nm to 12.3 μm to solve the radiation transport equation, where the radiative energy exchange between fluid elements is computed at all simulation time steps. The output consists of key plasma parameters, e.g., electron temperature, electron density, radiated power, etc., in the form of a 2D rotationally symmetric, infinitesimally thin “slice” of the center of the 3D plasma, an example being shown in Fig. 3. The second approach utilizes 235 unevenly spaced radiation groups from 0.6 to 332 nm, where the radiation transport equation is solved in the post-processor mode along one direction only at preselected time steps. To account for diffractive blurring, which is inherent to any imaging system, the pinhole and spectrometer impulse response function (IRF) were modeled using near-field Fresnel diffraction equations, which relies on the experimentally measured magnification, object and image distance, and aperture size.

In the first method, the following five-step procedure was applied to the simulation results: (i) 2D instantaneous emission profiles of six

adjacent wavelength bands in the region of interest were produced at 500 ps intervals from 0 to 15 ns (the laser temporal profile peaks at 7.5 ns). The wavelength bins have sequential edges at 0.62, 0.83, 1.13, 1.55, 2.07, 2.58, and 3.26 nm, which encompasses the majority of the experimentally observed emission. (ii) At each time step, the emission profile was Abel transformed: the experimental plasma images are a 2D projection of a 3D object. Due to the rotational symmetry of the RALEF-2D output, the simulation slice can be Abel transformed to give a 2D projection of the corresponding volume. This transformation is performed under the assumption of an optically thin medium. (iii) These emission profiles were then scaled with the wavelength-specific transmission scaling coefficient from the aluminum transmission filter. (iv) The scaled profiles were then convolved with the IRF of the pinhole imaging system and (v) finally summed for all wavelengths and all times.

The simulated and experimental plasma images and their characteristic lineouts perpendicular and parallel to the target are shown

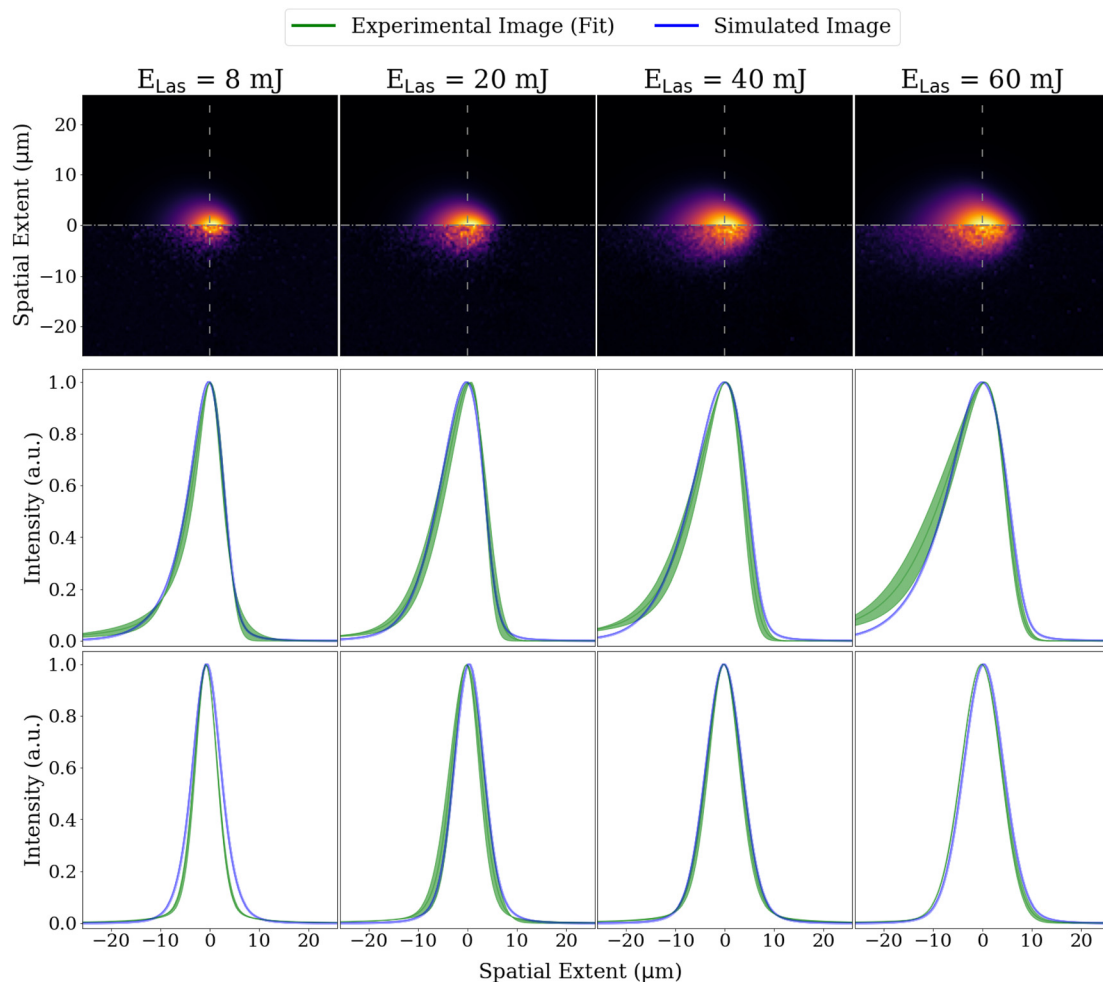


FIG. 4. Spatial profiles of the experimental and simulated plasma images. The top row consists of simulated (upper half) and experimental (lower half) plasma images. The second row shows lineouts taken through the center of the plasma (dash-dotted) that are perpendicular to the target. The bottom row shows lineouts taken through the center of the plasma image that are parallel to the target (dashed). Uncertainties are reflected in the shaded region (see main text). All lineouts are normalized to the peak values in the upper panel.

in Fig. 4. A remarkable agreement between experimental and simulated images both in scale and in shape is observed. The FWHM values and uncertainties of the experimental and simulated plasmas are shown in Fig. 5. Experimental error bars represent the spread of FWHM values across many images and the magnification uncertainty, which is also encapsulated by the green-filled region in Fig. 4. The simulated uncertainties shown capture the uncertainty in the IRF (which relies on experimentally measured values) and filter transmission. Given the good agreement between experimental and simulated plasma images, the true size of the plasma can be inferred directly from RALEF-2D, shown in red in Fig. 5. This circumvents the necessity of applying deconvolution models directly to the plasma images, which can be complex to implement, particularly with noisy plasma images. Figure 5 indicates that plasma size increases in both directions with increasing laser energy.

The second analysis method focused on spectra produced from the 1D numerical detector in RALEF-2D. The spectra for each laser energy produced by RALEF-2D were convolved with the transmission grating spectrometer IRF, the results of the highest power density case being shown in Fig. 2. Both experimental and modeled spectra show similar features, namely the three distinct emission peaks at 1.5, 1.8, and 2.4 nm. These experimental spectra have been compared to high-resolution experimental spectra taken at equivalent power densities, with good agreement concerning wavelength.⁴² A comparison with the work of Burkhalter *et al.*²⁶ indicates that the spectral features likely arise from Sn²²⁺ up to Sn²⁸⁺. This is consistent with the RALEF-2D calculated values, with sample contours of charge states shown in Fig. 3: the predicted

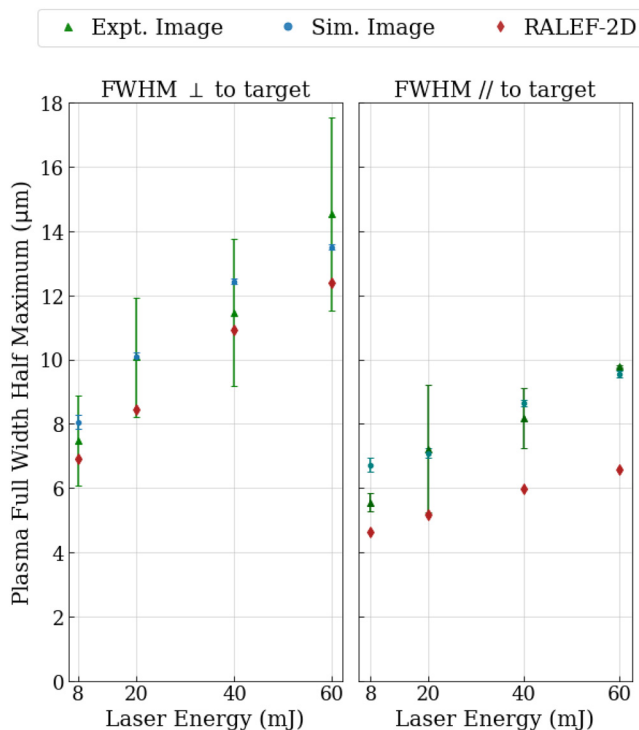


FIG. 5. Variation of the experimental (green) and simulated (blue) FWHM values of the plasma image lineouts, shown in Fig. 4 with increasing laser energy including uncertainty ranges (see the main text). Red diamonds show the RALEF-2D-predicted true plasma FWHM.

maximal ion stages from RALEF-2D for each laser energy are at least 22⁺, 25⁺, 27⁺, and 28⁺, respectively. The estimated power density used by Burkhalter *et al.* was approximately one order of magnitude higher than that in this work, and so the contributions are estimated to be reasonable from the simulation. Good agreement is observed between simulation and the experiment. The spatial discrepancy between simulation and experiment is mainly confined to the tails of the emission distribution. Spectrally, we observe only moderate differences in peak intensity ratios and positions. Considering the origin of such discrepancies, experimental uncertainties include the laser energy, which we estimate has an uncertainty of ~10% based on experimental measurements. The coverslip used to stop debris damaging the lens will likely acquire debris over time, and may introduce a minor attenuation of the laser beam. From RALEF-2D, it is possible a laser deposition model that accounts for the spatial expansion away from the target and opacity data better suited for 1064 nm ablation $\sim 10^{21} \text{ cm}^{-3}$ would produce better matching results. To summarize, the production and characterization of intense soft x-ray emission from tin LPPs driven by 1064-nm-wavelength laser pulses has been achieved experimentally. Radiation-hydrodynamic modeling using the RALEF-2D code has been demonstrated as a viable method of modeling the spatial and spectral behavior of tin LPP emission in the soft x-ray wavelength region at small scales, with good agreement despite the experimental uncertainties and model limitations. Intense soft x-ray emission features were observed at 1.5, 1.8, and 2.4 nm, with likely contributions from Sn²²⁺ up to Sn²⁸⁺ for the hottest plasmas generated. Given this agreement, inferences about plasma properties from radiation-hydrodynamic simulations can be made, such as the true plasma size and contributing ion stages. Spatial and spectral characterizations performed are essential for radiance calculations, which relies on knowledge of both spectral flux and plasma size. Future work will focus on the characterization of experimental and simulated conversion efficiencies and radiances, paving the way for predictive radiance determination.

This work was supported by the Science Foundation Ireland through a Frontiers for the Future Programme, Award No. 19/FFP/6795. Part of this work was performed at the Advanced Research Center for Nanolithography (ARCNL), a public-private partnership with founding partners UvA, VU, NWO-I, and ASML and associate partner RUG. This work made use of the Dutch national e-infrastructure with the support of the SURF Cooperative using Grant No. EINF-5992/L1. We highlight the contributions from the UCD School of Physics mechanical and electronic workshops who assisted in and facilitated large portions of the experimental construction and design, namely Richard Byrne and John Egan from the former and Jim McDaid and Robin O'Reilly from the latter. We thank Oscar Versolato for useful discussions and Jorge Gonzalez for his assistance in the modeling aspect of this work.

AUTHOR DECLARATIONS

Conflict of Interest

The authors have no conflicts to disclose.

Author Contributions

K. Mongey: Data curation (lead); Formal analysis (lead); Investigation (lead); Methodology (equal); Resources (equal); Software (equal);

Validation (equal); Visualization (lead); Writing – original draft (lead); Writing – review & editing (equal). **S. de Lange:** Investigation (supporting); Methodology (supporting); Software (supporting); Visualization (supporting); Writing – review & editing (supporting). **R. Brady:** Formal analysis (supporting); Investigation (supporting); Methodology (supporting); Software (equal); Validation (equal); Visualization (supporting); Writing – review & editing (supporting). **D. J. Hemminga:** Formal analysis (supporting); Software (supporting); Writing – review & editing (supporting). **B. Delaney:** Data curation (supporting); Formal analysis (supporting); Investigation (supporting); Methodology (supporting); Supervision (supporting); Writing – review & editing (supporting). **M. M. Basko:** Software (lead); Writing – review & editing (equal). **E. Sokell:** Conceptualization (equal); Funding acquisition (equal); Project administration (equal); Resources (equal); Supervision (equal); Writing – original draft (supporting); Writing – review & editing (equal). **F. O'Reilly:** Conceptualization (lead); Data curation (supporting); Formal analysis (equal); Funding acquisition (equal); Investigation (supporting); Methodology (equal); Project administration (equal); Resources (equal); Software (supporting); Supervision (equal); Validation (equal); Visualization (supporting); Writing – original draft (supporting); Writing – review & editing (equal). **J. Sheil:** Conceptualization (lead); Project administration (equal); Supervision (equal); Visualization (equal); Writing – original draft (supporting); Writing – review & editing (equal).

DATA AVAILABILITY

The data that support the findings of this study are available from the corresponding author upon reasonable request.

REFERENCES

- ¹G. O'Sullivan, B. Li, R. D'Arcy, P. Dunne, P. Hayden, D. Kilbane, T. McCormack, H. Ohashi, F. O'Reilly, P. Sheridan, E. Sokell, C. Suzuki, and T. Higashiguchi, *J. Phys. B: At. Mol. Opt. Phys.* **48**, 144025 (2015).
- ²*Short Wavelength Laboratory Sources: Principles and Practices*, edited by D. Bleiner, J. Costello, F. Dortan, G. O'Sullivan, L. Pina, and A. Michette (The Royal Society of Chemistry, London, 2014).
- ³H. Fiedorowicz, A. Bartnik, Z. Patron, and P. Parys, *Appl. Phys. Lett.* **62**, 2778 (1993).
- ⁴D. Bleiner, *Spectrochim. Acta, Part B* **181**, 105978 (2021).
- ⁵T. Higashiguchi, T. Otsuka, N. Yugami, W. Jiang, A. Endo, B. Li, P. Dunne, and G. O'Sullivan, *Appl. Phys. Lett.* **100**, 014103 (2012).
- ⁶M. A. van de Kerkhof, J. P. H. Benschop, and V. Y. Banine, *Solid-State Electron.* **155**, 20 (2019).
- ⁷O. O. Versolato, *Plasma Sources Sci. Technol.* **28**, 083001 (2019).
- ⁸F. Torretti, J. Sheil, R. Schupp, M. M. Basko, M. Bayraktar, R. A. Meijer, S. Witte, W. Ubachs, R. Hoekstra, O. O. Versolato, A. J. Neukirch, and J. Colgan, *Nat. Commun.* **11**, 2334 (2020).
- ⁹F. Torretti, R. Schupp, D. Kurilovich, A. Bayerle, J. Scheers, W. Ubachs, R. Hoekstra, and O. Versolato, *J. Phys. B: At. Mol. Opt. Phys.* **51**, 045005 (2018).
- ¹⁰M. Spanier, C. Herzog, D. Grötzsch, F. Kramer, I. Mantouvalou, J. Lubeck, J. Weser, C. Streeck, W. Malzer, B. Beckhoff, and B. Kanngießer, *Rev. Sci. Instrum.* **87**, 035108 (2016).
- ¹¹S. Staeck, A. Andrie, P. Hönicke, J. Baumann, D. Grötzsch, J. Weser, G. Goetzke, A. Jonas, Y. Kayser, F. Förste, I. Mantouvalou, J. Viefhaus, V. Soltwisch, H. Stiel, B. Beckhoff, and B. Kanngießer, *Nanomaterials* **12**, 3766 (2022).
- ¹²P. W. Wachulak, A. Bartnik, H. Fiedorowicz, P. Rudawski, R. Jarocki, J. Kostecki, and M. Szczurek, *Nucl. Instrum. Methods Phys. Res., Sect. B* **268**, 1692–1700 (2010).
- ¹³I. Mantouvalou, K. Witte, D. Grötzsch, M. Neitzel, S. Günther, J. Baumann, R. Jung, H. Stiel, B. Kanngießer, and W. Sandner, *Rev. Sci. Instrum.* **86**(3), 035116 (2015).
- ¹⁴M. Müller and K. Mann, *Nanoscale Photonic Imaging* (Springer International Publishing, Cham, 2020), pp. 549–559.
- ¹⁵K. A. Janulewicz, Ł. Węgrzyński, T. Fok, A. Bartnik, H. Fiedorowicz, S. Skruszewicz, M. Wünsche, E. Eckner, S. Fuchs, J. Reinhard, J. J. Abel, F. Wiesner, G. G. Paulus, C. Rödel, C. M. Kim, and P. W. Wachulak, *Opt. Express* **30**, 47867 (2022).
- ¹⁶A. Jonas, S. Staeck, B. Kanngießer, H. Stiel, and I. Mantouvalou, *Rev. Sci. Instrum.* **92**, 023102 (2021).
- ¹⁷G. Joseph, M. Olszewski, T. McCormack, P. Dunne, and F. O'Reilly, *Nucl. Instrum. Methods Phys. Res., Sect. B* **482**, 64 (2020).
- ¹⁸D. H. Martz, M. Selin, O. von Hofsten, E. Fogelqvist, A. Holmberg, U. Vogt, H. Legall, G. Blobel, C. Seim, H. Stiel, and H. M. Hertz, *Opt. Lett.* **37**, 4425 (2012).
- ¹⁹A. N. Nechay, A. A. Perekalov, N. N. Salashchenko, and N. I. Chkhalo, *Appl. Phys. B* **129**, 49 (2023).
- ²⁰R. Costantini, A. Morgante, and M. Dell'Angela, *J. Electron Spectrosc. Relat. Phenom.* **254**, 147141 (2022).
- ²¹J. Wang, M. Kishimoto, T. Jozaki, T. Kumeda, T. Higashiguchi, A. Sunahara, H. Ohiro, K. Yamasaki, and S. Namba, *Phys. Rev. E* **107**, 065211 (2023).
- ²²K. Fahy, V. Weinhardt, M. Vihinen-Ranta, N. Fletcher, D. Skoko, E. Pereiro, P. Gastaminza, R. Bartenschlager, D. Scholz, A. Ekman, and T. McEnroe, *J. Phys. Photonics* **3**, 031002 (2021).
- ²³C. John, M. Kishimoto, Y. Matsumoto, T. Morishita, T. Higashiguchi, T. Endo, A. Sunahara, T. Johzaki, and S. Namba, *High Energy Density Phys.* **37**, 100845 (2020).
- ²⁴M. M. Basko, *Phys. Plasmas* **23**, 083114 (2016).
- ²⁵D. J. Hemminga, O. O. Versolato, and J. Sheil, *Phys. Plasmas* **30**, 033301 (2023).
- ²⁶P. G. Burkhalter, U. Feldman, and R. D. Cowan, *J. Opt. Soc. Am.* **64**, 1058 (1974).
- ²⁷M. A. Khan, *J. Opt. Soc. Am.* **72**, 268 (1982).
- ²⁸Asphericon, Ah125-20 mm-u-u-780 nm asphere (2023).
- ²⁹IDS, U3-3682xle-nir rev.1.2 (2022).
- ³⁰A. D. Rakić, A. B. Djurišić, J. M. Elazar, and M. L. Majewski, *Appl. Opt.* **37**, 5271 (1998).
- ³¹ISO, International Standard. 1 (2005).
- ³²T. Harada, N. Teranishi, T. Watanabe, Q. Zhou, X. Yang, J. Bogaerts, and X. Wang, *Appl. Phys. Express* **12**, 082012 (2019).
- ³³W. M. Holden, O. R. Hoidn, G. T. Seidler, and A. D. Dichiara, *Rev. Sci. Instrum.* **89**, 093111 (2018).
- ³⁴B. L. Henke, E. M. Gullikson, and J. C. Davis, *At. Data Nucl. Data Tables* **54**, 181 (1993).
- ³⁵M. M. Basko, J. A. Maruhn, and A. Tauschwitz, "Development of a 2D radiation-hydrodynamics code RALEF for laser plasma simulations," GSI Report 2010-1, PLASMA-PHYSICS-25 (GSI Helmholtzzentrum für Schwerionenforschung GmbH, 2010).
- ³⁶M. M. Basko, P. V. Sasorov, M. Murakami, V. G. Novikov, and A. S. Grushin, *Plasma Phys. Control. Fusion* **54**, 055003 (2012).
- ³⁷F. L. Addessio, J. R. Baumgardner, J. K. Dukowicz, N. L. Johnson, B. A. Kashiwa, R. M. Rauenzahn, and C. Zemach, "CAVEAT: A computer code for fluid dynamics problems with large distortion and internal slip," Report No. LA-10613-MS-Rev. 1, UC-32 (Los Alamos National Laboratory, 1992).
- ³⁸E. Livne and A. Glasner, *J. Comput. Phys.* **58**, 59 (1985).
- ³⁹M. M. Basko, J. Maruhn, and A. Tauschwitz, *J. Comput. Phys.* **228**, 2175 (2009).
- ⁴⁰M. M. Basko and I. Tsygvintsev, *Comput. Phys. Commun.* **214**, 59 (2017).
- ⁴¹I. Yu. Vichev, A. D. Solomyannaya, A. S. Grushin, and D. A. Kim, *High Energy Density Phys.* **33**, 100713 (2019).
- ⁴²T. Miyazaki, "Spectroscopy of multiply charged fifth row ions from plasma sources," Ph.D. thesis (University College Dublin, 2022).